Chemical Engineering Journal 426 (2021) 131855

Contents lists available at ScienceDirect

Chemical Engineering Journal

journal homepage: www.elsevier.com/locate/cej

Highly efficient Pt catalyst on newly designed CeO_2-ZrO_2-Al_2O_3 support for catalytic removal of pollutants from vehicle exhaust

Wei Tan [a,b,1], Shaohua Xie [b,1], Xin Wang [a,1], Chunying Wang [c], Yaobin Li [c], Thomas E. Shaw [d], Lu Ma [e], Steven N. Ehrlich [e], Annai Liu [a], Jiawei Ji [a], Fei Gao [a,*], Lin Dong [a], Fudong Liu [b,*]

[a] Key Laboratory of Mesoscopic Chemistry of MOE, School of Chemistry and Chemical Engineering, Jiangsu Key Laboratory of Vehicle Emissions Control, School of Environment, Center of Modern Analysis, Nanjing University, Nanjing 210093, China
[b] Department of Civil, Environmental, and Construction Engineering, Catalysis Cluster for Renewable Energy and Chemical Transformations (REACT), NanoScience Technology Center (NSTC), University of Central Florida, Orlando, FL 32816, United States
[c] Key Laboratory of Urban Pollutant Conversion, Institute of Urban Environment, Chinese Academy of Sciences, Xiamen 361021, China
[d] Department of Chemistry, University of Central Florida, Orlando, FL 32816, United States
[e] National Synchrotron Light Source II (NSLS-II), Brookhaven National Laboratory, Upton, NY 11973, United States

ARTICLE INFO

Keywords:
Incipient wetness impregnation
Thermal stability
Pt single site catalyst
CO oxidation
Oxygen storage capacity

ABSTRACT

Pt-CeO_2 catalysts have been widely studied for the vehicle emission control. Designing novel CeO_2 based supports with improved physical-chemical properties has become a research hotspot to further promote the catalytic performance and stability of Pt-CeO_2 catalysts. In this work, through utilizing a unique, two-step incipient wetness impregnation (T-IWI) method for ceria-zirconia-alumina (CZA-T) support preparation, a Pt single site catalyst (Pt/CZA-T) with excellent thermal stability was synthesized. Higher oxidation activity and Oxygen storage capacity (OSC) were achieved on activated Pt/CZA-T, comparing to Pt catalysts on regular CeO_2/Al_2O_3 (Pt/CA) and one-step prepared $CeZrO_x$/Al_2O_3 (Pt/CZA). Via the modification of hydrophilic/hydrophobic properties of γ-Al_2O_3 by this unique T-IWI method, finer $Ce_{0.9}Zr_{0.1}O_2$ particles with higher density of surface defects were formed on CZA-T, on which a higher Pt dispersion and stronger Pt-O-Ce interaction were achieved. Upon activation, smaller, well-dispersed Pt clusters on CZA-T were generated. It was concluded that the CO oxidation performance and OSC were highly related to the size of Pt clusters on different supports that we have developed. More Pt sites located at Pt cluster-$CeZrO_x$ interfaces, which were the real active sites, were responsible for the highest OSC function and CO oxidation activity of activated Pt/CZA-T catalyst.

1. Introduction

Pollutants (CO, HCs and NO_x) emitted from automotive exhaust have serious impact on the ecological environment and human health [1]. With the tightening of emission control regulations and the widespread application of automotive cold-start emission control technology [2], current exhaust treatment catalysts require both improved low-temperature activity and thermal stability. Ceria based materials loaded with precious metals such as platinum (Pt) and palladium (Pd) have been widely used in catalytic CO and HCs oxidation due to their superior oxygen storage capacity and flexible valence states [3–7]. However, the thermal stability of pristine CeO_2 materials is still not satisfactory for practical application as they usually suffer from severe sintering and surface area loss at high aging temperatures such as above 800 °C [8]. Many strategies have been developed to improve the thermal stability of CeO_2, such as the modification with alkaline earth or transition metals (Ba, Zr, Ti *etc.*), or loading CeO_2 on other stable refractory oxide supports [9,10]. Coupled with the stability issue, another industrially relevant concern is the cost-effectiveness of the catalyst if using pristine CeO_2 as support. As one of the rare earth elements, cerium has limited reserves and is relatively more expensive than base metals such as γ-Al_2O_3 [11]. Although much progress has already been made towards the improvement of reactivity and stability of precious metal catalysts loaded on CeO_2 [12–14], achieving the balance between CeO_2 usage reduction, improving thermal stability, and maintaining superior catalytic activity is still a big challenge in environmental catalysis area.

* Corresponding authors.
E-mail addresses: gaofei@nju.edu.cn (F. Gao), fudong.liu@ucf.edu (F. Liu).
[1] Wei Tan, Shaohua Xie and Xin Wang contributed equally to this work.

https://doi.org/10.1016/j.cej.2021.131855
Received 4 May 2021; Received in revised form 7 August 2021; Accepted 11 August 2021
Available online 18 August 2021

To address the above-mentioned thermal stability issue, CeO_2 loaded on γ-Al_2O_3 has been widely used as catalyst supports in previous work by other researchers [15–18]. For example, Jeong *et al.* loaded Pt, Pd and Rh onto reduced γ-Al_2O_3 supported CeO_2, on which the highly dispersed metal ensemble catalysts exhibited superior catalytic performance and stability in three-way catalysis (TWC) reaction [17]. The synergic stabilization effect between CeO_2 and γ-Al_2O_3 could help retard the sintering of CeO_2 on γ-Al_2O_3 [19]. At the same time, the phase transformation of γ-Al_2O_3 to α-Al_2O_3 or θ-Al_2O_3 could also be hindered by CeO_2 modification [19,20]. It must be noted that, in environmental catalysis field, great efforts have also been made on improving the thermal stability and oxygen storage capacity (OSC) of CeO_2 itself. The doping of other metals such as Zr, Y, Pr, Nd, Ga and La [20–23] was a common strategy to enhance the thermal stability or OSC function of CeO_2. Particularly, the effects of Zr doping on CeO_2 have been widely studied, with notable improvements on the thermal stability and oxygen storage/release properties of CeO_2 [24–27]. For example, Zhang *et al.* found that Zr doping in Ni/CeO_2 catalysts could improve the catalytic activity and H_2 selectivity in methane dry reforming [25]. Liu *et al.* reported that the addition of Zr could increase the amount of oxygen vacancies in CeO_2 rods, further improving the catalytic activity for dimethyl carbonate (DMC) synthesis from CO and methane [26]. It was also reported that Zr doped Au/CeO_2 showed better CO oxidation activity than those with Fe or La doping [27]. Although Pt/CeO_2 catalysts have been investigated extensively in a variety of catalytic processes such as CO/HCs oxidation reactions [13,28–30] and water-gas shift reaction [31], and the relationship between the Pt status on CeO_2 surface and its catalytic performance has been well revealed, however, few studies have focused on the impact of ZrO_2 doping on the Pt dispersion and Pt-CeO_2 interaction thus affecting catalytic performance.

In this study, a new strategy was proposed to improve the catalytic performance of Pt catalysts loaded on CeO_2 while simultaneously reducing the usage amount of CeO_2. Through the co-deposition of Ce-Zr mixed precursor onto γ-Al_2O_3 using a new two-step incipient wetness impregnation (T-IWI) method, the surface hydrophilic/hydrophobic properties of γ-Al_2O_3 were effectively modified and a novel γ-Al_2O_3 supported $CeZrO_x$ with unique morphology was obtained. Pt supported on such support showed relatively higher CO oxidation activity and thermal stability after activation treatment by H_2 reduction. After the introduction of water vapor into the reactant stream, the CO oxidation activity on this novel catalyst even showed significant increase. Comparing to the heavily reported pristine CeO_2 support, the CeO_2 usage amount in such catalyst was significantly reduced while the catalytic performance was actually improved, implying that the catalysts developed in this work can be more cost-effective with great potential in practical application. Furthermore, it was found that the dispersion state of Pt and the intensity of Pt-CeO_2 interaction on CeO_2/γ-Al_2O_3 support could be well regulated by ZrO_2 doping through the new T-IWI method.

2. Experimental

2.1. Catalyst preparation

2.1.1. Preparation of CeO_2/Al_2O_3 and $CeZrO_x/Al_2O_3$ supports

30 wt% CeO_2 ($Ce(NO_3)_3{\cdot}6H_2O$ as precursor) was loaded on a commercial γ-Al_2O_3 provided by Sasol using a regular incipient wetness impregnation (IWI) method, followed by calcination at 550 °C for 2 h. The obtained CeO_2/Al_2O_3 support was denoted as CA. The Zr-doped CeO_2/Al_2O_3 support was prepared by the same IWI method, yet a mixed solution of $Ce(NO_3)_3{\cdot}6H_2O$ and $ZrO(NO_3)_2{\cdot}6.5H_2O$ (the molar ratio of Ce to Zr was 9:1 while keeping the mass ratio of $CeZrO_x$ still as 30 wt%) was used instead. The obtained $CeZrO_x/Al_2O_3$ support was denoted as CZA. For the improved $CeZrO_x/Al_2O_3$ support used in this work, the above-mentioned mixed precursor was loaded onto γ-Al_2O_3 in two steps. First, 10 wt% $Ce_{0.9}Zr_{0.1}O_2$ was deposited onto γ-Al_2O_3 followed by calcination at 800 °C for 2 h (10CZA-800). Then, another 20 wt % $Ce_{0.9}Zr_{0.1}O_2$ was deposited onto 10CZA-800 followed by calcination at 550 °C for 2 h. The obtained support herein was denoted as CZA-T, and such procedure was referred as T-IWI method.

2.1.2. Preparation of Pt catalysts supported on CeO_2/Al_2O_3 and $CeZrO_x/Al_2O_3$

Tetraamineplatinum nitrate ($Pt(NH_3)_4(NO_3)_2$, TAPN) obtained from Fisher Scientific was used as Pt precursor, which was deposited onto the different supports by IWI method. The Pt loading was set at 1 wt%. In a typical procedure, the Pt precursor with determined concentration was added dropwise onto CA, CZA, or CZA-T, and the obtained powder was dried at 120 °C for 1 h and then calcined at 550 °C for 2 h under air condition. The as-prepared catalysts were denoted as 1Pt/CA, 1Pt/CZA and 1Pt/CZA-T. To investigate thermal stability, the as-prepared 1Pt/CA, 1Pt/CZA and 1Pt/CZA-T catalysts were aged at 800 or 1000 °C in air for 12 h. The aged catalysts were denoted as 1Pt/CA-800A, 1Pt/CZA-800A, 1Pt/CZA-T-800A, 1Pt/CA-1000A, 1Pt/CZA-1000A and 1Pt/CZA-T-1000A. To study the hydrothermal stability, the catalysts were treated in a flow of air with 10% H_2O at 800 °C for 12 h, and the hydrothermally aged samples were denoted as 1Pt/CA-HA, 1Pt/CZA-HA and 1Pt/CZA-T-HA.

Before activity testing, each catalyst was pressed into pellet, then crushed and sieved into 40–60 meshes. All the catalysts were pretreated in air at 300 °C (for cleaning the catalyst surface) or 10% H_2/Ar flow at 400 °C (for reduction activation) for 1 h, with a total flow rate of 30 sccm. For the catalysts pretreated with H_2, '-a' was suffixed after the sample name. To facilitate a better understanding of the catalyst preparation process, the preparation flow chart can be found in Fig. S1.

2.2. Catalyst characterization

The atomic resolution high angle dark field scanning transmission electron microscopy (HAADF-STEM) images and the energy dispersive spectroscopy (EDS) elemental mapping images were obtained on a fifth order aberration-corrected transmission electron microscope (JEOL ARM200CF) equipped with a dual-type EDS detector (JED-2300 T, large effective solid angle at *ca.* 1.2 sr.).

Water contact angle measurements for the supports prepared in this work were conducted on an Ossila water contact angle goniometer.

X-ray powder diffraction (XRD) patterns were collected on a Philips X'pert Pro diffractometer with a Ni-filtered Cu Kα radiation source (0.15408 nm). The XRD patterns were collected over a 2θ range of 20–80 °. The scan step was 0.02° with a scan speed of 10°/min.

The specific surface area was measured by the Brunaeur, Emmett and Teller (BET) method (Quantachrome Autosorb-iQ Physisorption Chemisorption Instrument) using N_2 adsorption–desorption isotherms at 77.3 K. Before each test, the samples were degassed at 300 °C for 2 h.

Raman spectra were collected on a LabRAM Aramis (Japan Horiba) Laser Raman spectrometer equipped with an Ar^+ laser beam. The emission line was set at 532 nm and the laser power was 10 mW.

X-ray absorption spectroscopy (XAS) for Pt L_3-edge were measured in fluorescence mode at beamline 7-BM QAS of the National Synchrotron Light Source II (NSLS-II) at Brookhaven National Laboratory. The beamline could provide X-ray with energies ranging from 4.7 to 31 keV. Its monochromator has a Si(1 1 1) channel-cut crystal and runs at continuous scan mode. A typical scan time was 40 s and each sample was scanned 20 times. The XAS data including X-ray absorption near edge structure (XANES) and extended X-ray absorption fine structure (EXAFS) were analyzed using Demeter software package.

H_2-temperature-programed reduction (H_2-TPR) was performed on a Quantachrome Autosorb-iQ instrument. In each test, sample (*ca.* 30 mg) was pretreated with air at 400 °C for 1 h. Then the sample was cooled down to room temperature in air. After switching the purging gas to H_2 (10 % H_2/Ar, 30 mL/min), the temperature was linearly raised from 30 to 900 °C with a ramping rate of 10 °C/min. The signal of H_2 consumption was collected by a thermal conductivity detector (TCD). H_2O

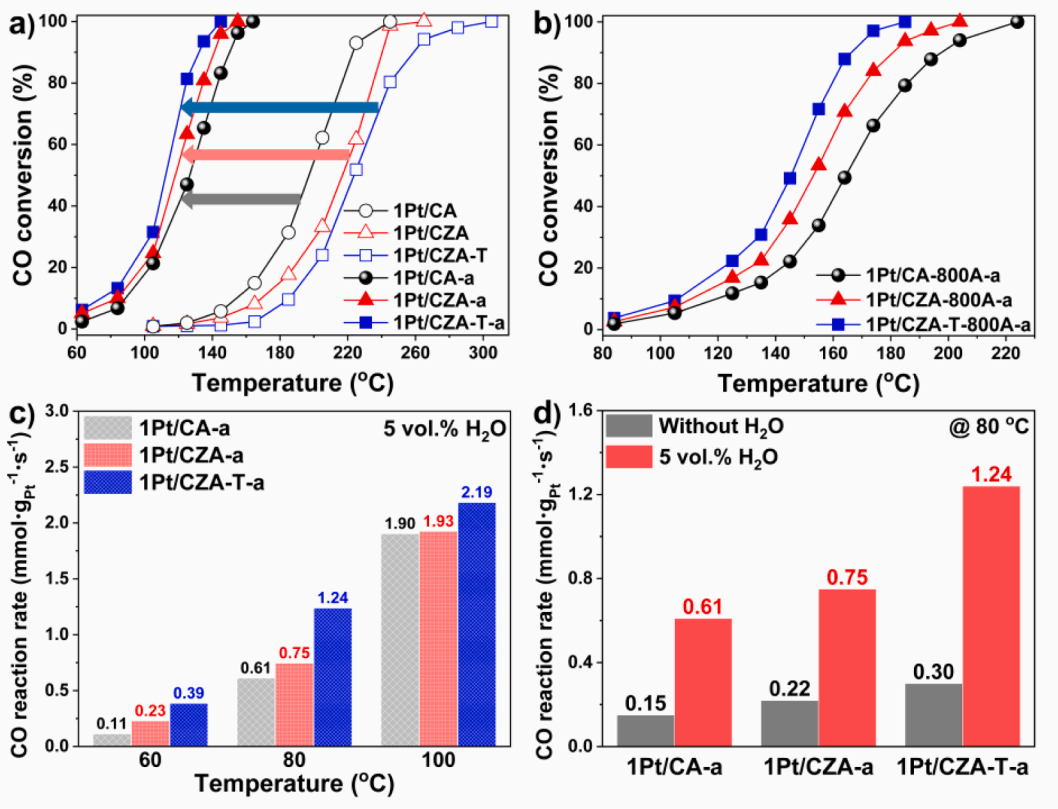

Fig. 1. CO oxidation activity on a) as-prepared catalysts pretreated with air at 300 °C or activated with 10% H_2 at 400 °C and b) aged catalysts (800 °C in air for 12 h) activated with 10% H_2 at 400 °C; c) CO oxidation rates at different temperatures on activated as-prepared catalysts with 5 vol% H_2O in the reactants; d) CO oxidation rates at 80 °C on activated as-prepared catalysts with or without 5 vol% H_2O in the reactants.

was removed by a cold trap filled with liquid N_2 before the gas mixture passed into the TCD.

X-ray Photoelectron Spectroscopy (XPS) were measured on a PHI 5000 Versa Probe system with a monochromatic Al X-ray radiation (1486.6 eV) and an accelerating power of 15 kW. Binding energies (BE) of all the elements were calibrated with C1s at 284.6 eV.

The oxygen storage capacity (OSC) was measured in CO/O_2 multi-pulse experiments. After the activation treatment by H_2 at 400 °C for 1 h, the catalysts were heated to the target temperatures (80, 100, 120, 140 °C) under alternating pulses of 2% CO/4% O_2 (total flow rate of 100 sccm) for 30 min, with a single cycle lasting 1 min (30 s CO/30 s O_2 cycling switch controlled by programmed MFC system). The OSC value was calculated from the average CO_2 formation which was detected by an online mass spectrometer (Hiden Analytical, HPR20 R&D).

In situ diffuse reflectance infrared Fourier transform spectroscopy (*in situ* DRIFTS) was carried out on a Thermo Nicolet iS50 FTIR spectrometer equipped with an MCT detector. The experiment started by loading the catalyst in the DRIFTS cell, where *ca.* 30 mg of the catalyst was pressed and mounted. Before testing, the catalysts were pretreated by air at 300 °C or 10% H_2/Ar at 400 °C for 1 h. Afterwards, the catalysts were cooled to room temperature. The backgrounds of the catalysts were collected in air or Ar at 25 °C, 50 °C and 100 °C. For CO adsorption/oxidation experiments, the feeding gas was controlled at a rate of 83.3 sccm (1% CO when needed, or 1% O_2 when needed; balanced with Ar). The spectra were collected from 400 to 4000 cm^{-1} at a spectral resolution of 4 cm^{-1} for 100 scans. The DRIFTS data were presented in the form of absorbance.

2.3. Catalytic performance test

Catalytic performance evaluation was conducted on a fixed-bed quartz tube reactor. In each test, 25 mg of sample (40–60 mesh) was diluted with 250 mg SiC to minimize the heat effect. The oxidation activity was tested under steady conditions. For CO oxidation, the reactants consisted of 1% CO, 1% O_2 and/or 5 vol% H_2O (when needed), balanced with Ar. For propane (C_3H_8) oxidation, the reactants were composed of 2000 ppm C_3H_8, 2% O_2 and/or 5 vol% H_2O (when needed), balanced with Ar. For both reactions, the total flow rate was 83.3 sccm, giving a weight hourly space velocity (WHSV) of 200,000 mL·g$_{cat.}^{-1}$·h^{-1}). The outlet gas composition was measured by an online mass spectrometer. The mass to charge (m/z) ratios used for the detection of CO, CO_2 and C_3H_8 were 28, 44 and 29, respectively.

3. Results and discussion

3.1. Catalytic performance for CO and C_3H_8 oxidation

The CO oxidation activity of catalysts before and after reduction activation is shown in Fig. 1a. For the catalysts pretreated with air at 300 °C, 1Pt/CA exhibited the best CO oxidation activity with T90, the temperature at which CO conversion reaches 90%, of *ca.* 222 °C, which was much lower than those on 1Pt/CZA and 1Pt/CZA-T (*ca.* 240 and 258 °C, respectively). The CO oxidation activity of these three catalysts was greatly enhanced after H_2 pretreatment, which was highly consistent with the reports that the activation treatment by reductive gases could enhance the CO oxidation performance of Pt/CeO_2 catalysts [13,28]. Interestingly, the order of CO oxidation activity over the activated catalysts was completely reversed comparing to that over the as-prepared catalysts. Specifically, 1Pt/CZA-T-a showed an excellent CO oxidation activity with T90 of *ca.* 130 °C, which was much lower than that on 1Pt/CA-a (*ca.* 150 °C) and 1Pt/CZA-a (*ca.* 140 °C). The reaction rates of CO oxidation over the activated catalysts at 120 °C were also calculated, with a rate of 1.01 mmol g_{Pt}^{-1}·s^{-1} for 1Pt/CA-a, 1.32 mmol g_{Pt}^{-1}·s^{-1} for 1Pt/CZA-a, and 1.71 mmol g_{Pt}^{-1}·s^{-1} for 1Pt/CZA-T-a.

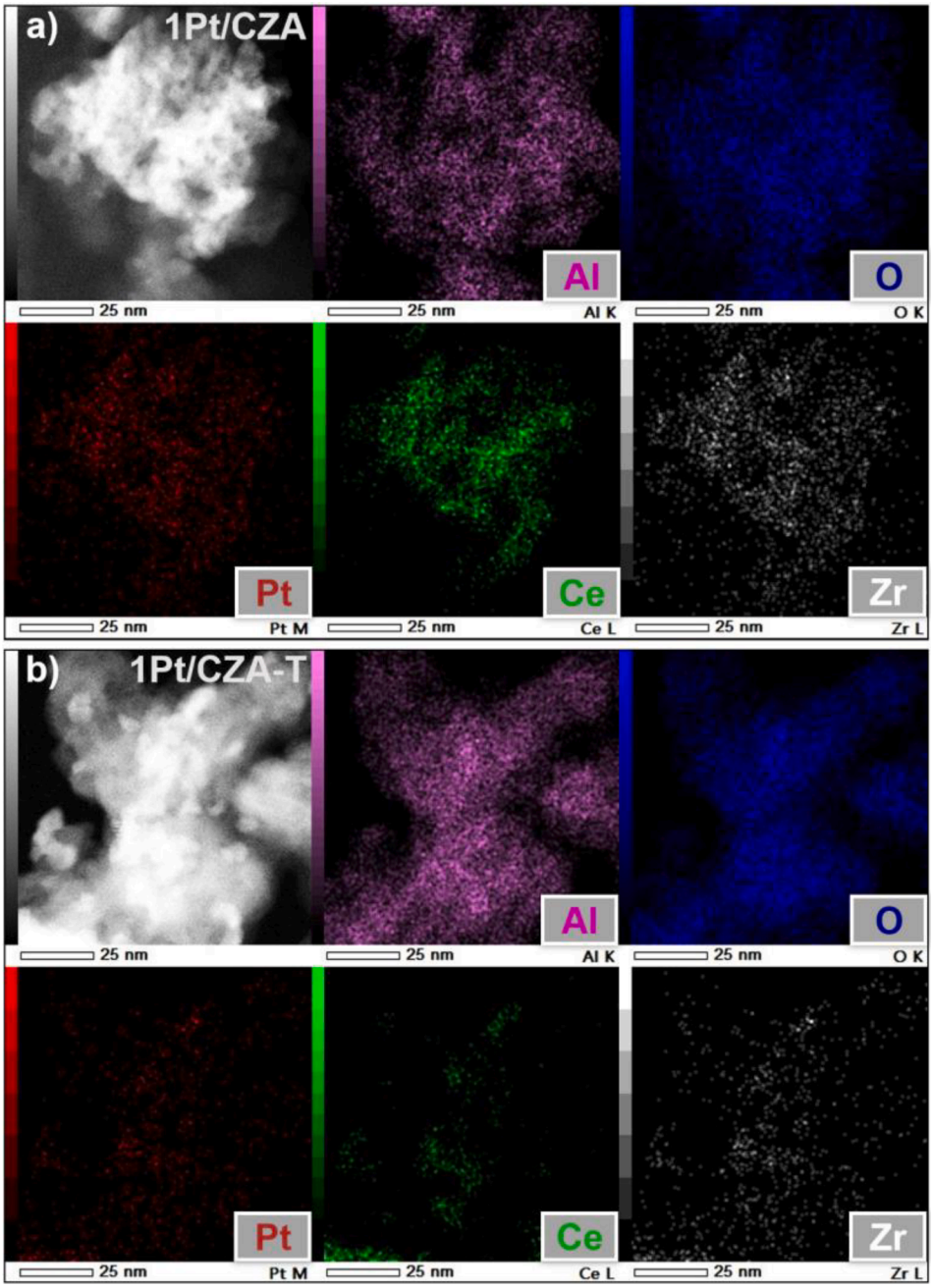

Fig. 2. HAADF-STEM images and EDS mapping results of a) 1Pt/CZA and b) 1Pt/CZA-T.

Recent work has highlighted the promising applications of Pt/CeO_2 catalysts in vehicle emission control [13,28,32]. Therefore, for comparison, 1 wt% Pt/CeO_2 catalyst (denoted as $1Pt/CeO_2$, with CeO_2 obtained from $Ce(NO_3)_3{\cdot}6H_2O$ precursor through calcination at 550 °C for 2 h) was also prepared following the same Pt loading procedure and tested for CO oxidation (Fig. S2a). It is obvious that 1Pt/CZA-T-a exhibited much higher CO oxidation activity than $1Pt/CeO_2$-a at temperature above 120 °C, *e.g.* the T90 on 1Pt/CZA-T-a being *ca.* 65 °C lower than that on $1Pt/CeO_2$-a. To further compare the CO oxidation activity of 1Pt/CZA-T-a catalyst with recently reported Pt-CeO_2 based catalysts, the T50, T90 (the temperature at which CO conversions reached 50% and 90%, respectively) and CO oxidation rate at 80 °C on these novel catalysts were summarized and listed in Table S1. The 1Pt/CZA-T-a catalyst developed in this work performed as one of the best among those novel catalysts. Furthermore, the usage of CeO_2 in 1Pt/CZA-T-a was reduced by 70%, which made it more cost-effective.

Thermal stability is also an important factor in evaluating a catalyst for vehicle emission control applications. In this work, the CO oxidation activity of 1Pt/CA, 1Pt/CZA and 1Pt/CZA-T catalysts with different aging temperatures (800 and 1000 °C) was tested. After aging at 800 °C for 12 h (Fig. 1b), the CO oxidation activities of all the catalysts decreased to a certain extent. Their activities were in the order of 1Pt/CZA-T-800A-a > 1Pt/CZA-800A-a > 1Pt/CA-800A-a. Among all the aged catalysts, 1Pt/CZA-T-800A-a with T90 of *ca.* 165 °C still exhibited the highest CO oxidation activity. Similarly, even after severe aging at 1000 °C for 12 h, 1Pt/CZA-T-1000A-a catalyst still performed the best (Fig. S2b). Hydrothermal aging treatment (in air with 10 vol% H_2O at 800 °C for 12 h) was conducted on 1Pt/CA, 1Pt/CZA and 1Pt/CZA-T to further investigate their hydrothermal stability. As shown in Fig. S3, CO oxidation activity on 1Pt/CZA-T-HA-a was still higher than that on 1Pt/CZA-HA-a and 1Pt/CA-HA-a. Apparently, CZA support prepared via the new T-IWI method enabled the highly active 1Pt/CZA-T catalyst for CO

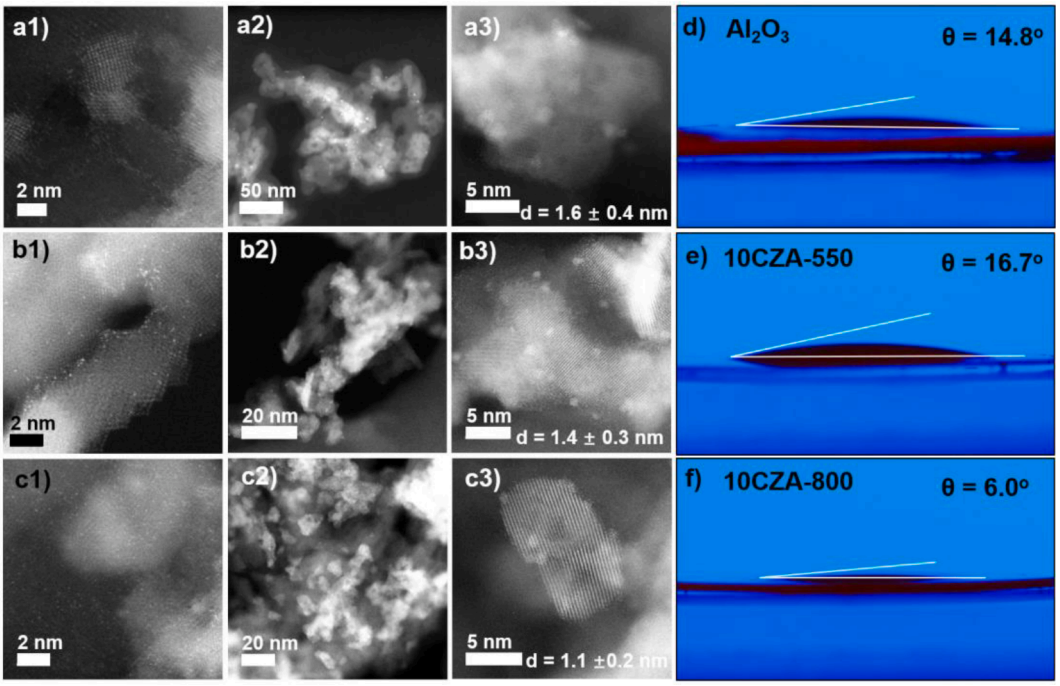

Fig. 3. HAADF-STEM images of a1) 1Pt/CA, b1) 1Pt/CZA and c1) 1Pt/CZA-T; HAADF-STEM images of a2, a3) 1Pt/CA-a, b2, b3) 1Pt/CZA-a and c2, c3) 1Pt/CZA-T-a; Water contact angle on d) γ-Al_2O_3, e) 10CZA-550 and f) 10CZA-800.

oxidation even after severe aging treatment. As a typical hydrocarbon component in gasoline exhaust, propane (C_3H_8) was also selected for evaluating the oxidation performance on the aged catalysts. It can be observed from Fig. S4a that 1Pt/CZA-T-800A-a catalyst exhibited higher C_3H_8 oxidation activity than 1Pt/CZA-800A-a and 1Pt/CA-800A-a, indicating that the novel T-IWI method was indeed beneficial for generating a more thermally stable oxidation catalyst. 1Pt/CZA-T-800A-a also exhibited the highest CO_2 selectivity (Fig. S4b). In short summary, the strategy of combining Zr doping and T-IWI approach could significantly boost the catalytic oxidation performance of $Pt/CeO_2/Al_2O_3$ catalyst as well as the thermal stability.

In the real working conditions, H_2O was one of the most abundant molecules in the vehicle exhaust. Herein, the impact of H_2O on the CO oxidation activity on 1Pt/CA-a, 1Pt/CZA-a and 1Pt/CZA-T-a was further investigated. As shown in Fig. 1c and Fig. S5, with 5 vol% H_2O in the reactant stream, 1Pt/CZA-T-a catalyst still performed much better than 1Pt/CZA-a and 1Pt/CA-a. Interestingly, after the introduction of 5 vol% H_2O, the CO oxidation activity was not inhibited but significantly enhanced, indicating that 1Pt/CZA-T-a was highly compatible to working conditions containing water vapor. As reported by Wang *et. al.*, the formation of hydroxyl groups on Pt/CeO_2 catalyst could facilitate the formation of CO_2 [33]. Nie *et al.* also supported the view that hydroxyl groups on Pt/CeO_2 catalysts contributed to the activation of oxygen species, which promoted the CO oxidation activity of Pt/CeO_2 [5]. H_2O is more of a promoter in CO oxidation reaction on Pt/CeO_2 based catalysts. For propane oxidation reaction on 1Pt/CA-a, 1Pt/CZA-a and 1Pt/CZA-T-a catalysts, no significant change in catalytic activity was observed with 5 vol% H_2O in the reactant stream (Fig. S4c and d), with 1Pt/CZA-T-a still showing the highest performance among the three catalysts.

3.2. Structure information

3.2.1. HAADF-STEM and EDS mapping to determine support morphology and Pt status

HAADF-STEM and EDS mapping analysis were first conducted to determine the distribution of Pt, Zr, or Ce on γ-Al_2O_3 for all as-prepared catalysts. As shown in Figs. S6 and 2a, Al_2O_3 supported CeO_2 or $CeZrO_x$ particles with diameters > 20 nm were observed on 1Pt/CA and 1Pt/CZA. For 1Pt/CZA and 1Pt/CZA-T, ZrO_2 was found to be well mixed with CeO_2, indicating that a homogeneous Ce-Zr mixed oxide was formed on the surface of Al_2O_3 (Fig. 2). However, different from 1Pt/CZA (Fig. 2a) and 1Pt/CA (Fig. S6), much smaller $Ce_{0.9}Zr_{0.1}O_2$ particles (5–10 nm) were formed on 1Pt/CZA-T (Fig. 2b), indicating that the newly developed T-IWI method was beneficial for reducing the $Ce_{0.9}Zr_{0.1}O_2$ particle size. It is noteworthy that, the distribution of Pt species was in well tracking with the distribution of Ce and Zr, which indicated that the Pt species were primarily anchored on CeO_2 or $Ce_{0.9}Zr_{0.1}O_2$ entities on Al_2O_3 surface.

Detailed HAADF-STEM images with atomic-level resolution were captured to further investigate the status Pt species on as-prepared and activated catalysts. As illustrated in Figs. 3 and S7, before the activation treatment, Pt species were well dispersed on CA, CZA and CZA-T supports mainly in the form of single sites, while several distinct Pt clusters were also found on 1Pt/CA (Fig. S7a). This indicated that the addition of ZrO_2 to CeO_2 could further facilitate the dispersion of Pt on CeO_2 exclusively in the form of single sites, probably due to the creation of more surface defects on CeO_2 surface for Pt anchoring. For 1Pt/CA, 1Pt/CZA and 1Pt/CZA-T activated by H_2 reduction, a large amount of Pt clusters with average size below 2 nm could be observed on the different supports. Considering the higher activity of as-prepared 1Pt/CA comparing to 1Pt/CZA and 1Pt/CZA-T as well as the significant activity enhancement by reduction activation, the Pt clusters on CeO_2 or $Ce_{0.9}Zr_{0.1}O_2$ entities should be more active for CO oxidation than Pt single sites.

As shown in Figs. 3 and S8, it was noticed that the size of Pt clusters formed on different supports after activation varied significantly. The average sizes of Pt clusters within 1Pt/CA-a, 1Pt/CZA-a and 1Pt/CZA-T-a were statistically calculated as 1.6 ± 0.4 nm, 1.4 ± 0.3 nm, and 1.1 ± 0.2 nm, respectively. Considering that the activation conditions were held constant, the interaction between Pt species and different supports in as-prepared catalysts should dominate the formation of distinct Pt clusters during H_2 reduction activation. The smallest Pt cluster size was found on Pt/CZA-T-a, indicating the strongest interaction between Pt

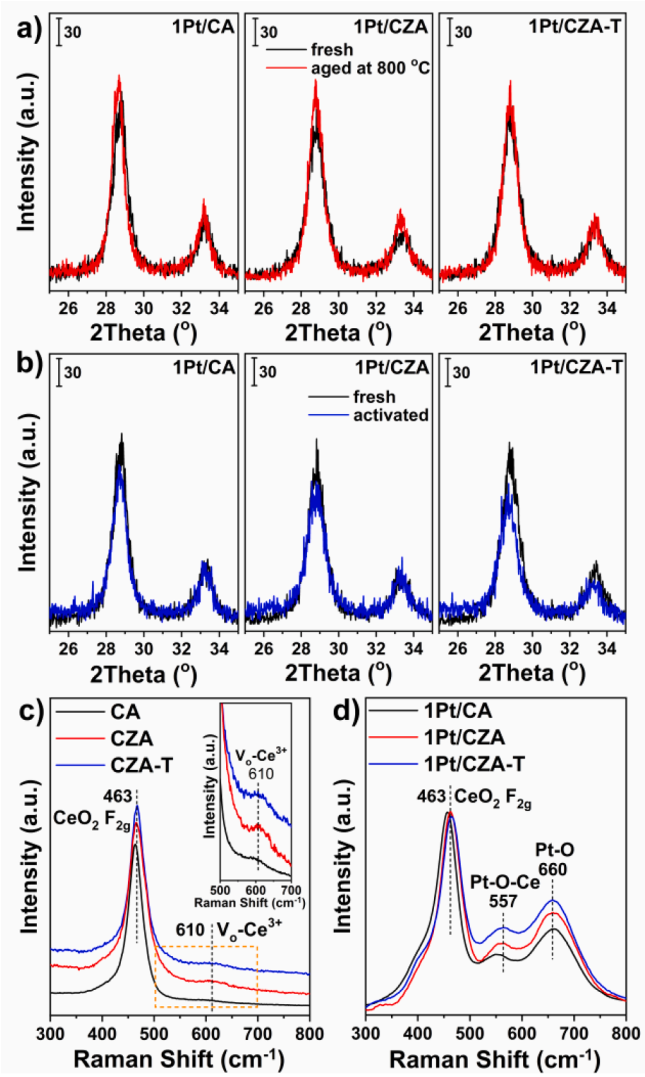

Fig. 4. XRD patterns for a) fresh and aged (800 °C in air for 12 h) 1Pt/CA, 1Pt/CZA and 1Pt/CZA-T catalysts; b) fresh and activated (400 °C in 10% H_2 for 1 h) 1Pt/CA, 1Pt/CZA and 1Pt/CZA-T catalysts. Raman spectra for c) CA, CZA and CZA-T supports; d) as-prepared 1Pt/CA, 1Pt/CZA and 1Pt/CZA-T catalysts.

single sites and CZA-T support.

As reported in literature, the strong metal-support interaction (SMSI) is highly dependent on the morphology of the studied supports [34,35]. As demonstrated in Fig. 3-a2and b2, CeO_2 and $Ce_{0.9}Zr_{0.1}O_2$ particles > 20 nm could be found on 1Pt/CA-a and 1Pt/CZA-a, while abundant small $Ce_{0.9}Zr_{0.1}O_2$ particles within the range of 5–10 nm could be observed on 1Pt/CZA-T-a (Figs. 3-c2). Moreover, a higher density of small Pt clusters (~1 nm) was found at the edges of $Ce_{0.9}Zr_{0.1}O_2$ particles within 1Pt/CZA-T-a catalyst. Kunwar *et al.* reported that Pt species tended to be anchored at the step edges of CeO_2 for efficient stabilization [28]. Dvořák et al. also reported that the step edges, the most common surface defects on oxide supports, were very important for single-atom Pt stabilization [36]. In our study, CZA-T support prepared by the new T-IWI method possessed smaller $Ce_{0.9}Zr_{0.1}O_2$ particles on Al_2O_3 surface with rich step edges, which was very beneficial for the anchoring of Pt single sites. The Pt single sites anchored on such step edges were quite stable, which could be transformed into highly active small Pt clusters for oxidation reactions after H_2 reduction activation.

Table 1
CeO_2 crystalline size and BET surface area for all catalysts and different supports.

Samples	Crystalline size of as-prepared samples/nm [a]	Crystalline size of activated samples/nm [a]	BET surface area/ (m^2/g) [b]
1Pt/CA	10.8	10.7	100
1Pt/CZA	9.1	8.9	91
1Pt/CZA-T	9.1	8.1	84
1Pt/CA-800A	12.5	/	69
1Pt/CZA-800A	10.6	/	69
1Pt/CZA-T-800A	9.8	/	75
CA	10.3	/	98
CZA	9.0	/	96
CZA-T	9.1	/	85

[a] The crystalline size was calculated by Scherrer equation, using CeO_2 (1 1 1).
[b] The specific surface areas of as-prepared samples were measured by N_2 physisorption at −196 °C.

3.2.2. *Contact angle of H_2O to determine surface Hydrophilicity/Hydrophobicity*

According to the results of HAADF-STEM and EDS mapping, a significant difference was observed for the $Ce_{0.9}Zr_{0.1}O_2$ particle sizes on CZA and CZA-T, where the $Ce_{0.9}Zr_{0.1}O_2$ particles on CZA-T were much smaller than those on CZA. Since the CZA and CZA-T supports were prepared by IWI method, the hydrophilicity/hydrophobicity of the substrates (*i.e.,* γ-Al_2O_3 for CZA or 10CZA-800 for CZA-T) would greatly affect the wetness and dispersion of Ce-Zr mixed precursor ($Ce(NO_3)_3{\cdot}6H_2O$ + $ZrO(NO_3)_2{\cdot}6.5H_2O$) on such substrate surfaces. It has been reported that hydrophilic surface would facilitate the adsorption of aqueous solution [37]. On a more hydrophilic substrate, the impregnated aqueous solution of Ce-Zr mixed precursor could highly disperse on substrate surface, which would lead to the formation of more homogeneously dispersed small $Ce_{0.9}Zr_{0.1}O_2$ particles upon final calcination.

The water contact angle experiments were conducted to evaluate the hydrophilicity/hydrophobicity of γ-Al_2O_3, 10CZA-550 (*i.e.*, 10 wt% $Ce_{0.9}Zr_{0.1}O_2/Al_2O_3$ calcined at 550 °C for 2 h) and 10CZA-800. As shown in Fig. 3d and 3e, the water contact angles on Al_2O_3 and 10CZA-550 were *ca.* 14.8 and 16.7°, respectively. However, the contact angle for 10CZA-800 was only 6.0° (Fig. 3f), indicating that the surface of 10CZA became more hydrophilic due to the high temperature calcination at 800 °C. It has been reported that calcining CeO_2-Al_2O_3 at relatively higher temperatures could facilitate the formation of more surface −OH groups, which could improve the hydrophilicity [38], and the higher hydrophilicity was related to the stronger interaction between H_2O molecules and metal oxide surfaces [39]. Such a hydrophilic surface of 10CZA-800 would positively promote the dispersion of second-step deposited Ce-Zr precursor solution for the additional loading of 20 wt % $Ce_{0.9}Zr_{0.1}O_2$. As expected, the high dispersion degree of Ce-Zr precursor solution was indeed beneficial for the formation of smaller $Ce_{0.9}Zr_{0.1}O_2$ particles on CZA-T upon calcination, which was already verified by HAADF-STEM and EDS mapping results.

3.2.3. *XRD and BET surface area to determine the crystal and textural properties*

As shown in Figs. 4a and S9a, the XRD patterns of 1Pt/CA, 1Pt/CZA and 1Pt/CZA-T displayed mixed crystal structures of cubic fluorite CeO_2 and γ-Al_2O_3. No diffraction peaks of ZrO_2 was detected, indicating that Zr was well doped into CeO_2 matrix without forming large aggregates. In addition, the peaks assigned to Pt species could hardly be observed from the XRD patterns, demonstrating that Pt species was well dispersed on CA, CZA and CZA-T supports, in well accordance with the HAADF-STEM and EDS mapping results. After aging at 800 °C, the intensity of CeO_2

Table 2
Data summary on the parameters of Raman spectra, XPS and *in situ* DRIFTS of CO adsorption.

Samples	Raman spectra parameters					Peak parameters at 2098 cm^{-1}		
	$I_{(Pt\text{-}O)}/I_{(F2g)}$[a]	Ratio decrease[a]	$I_{(Pt\text{-}O\text{-}Ce)}/I_{(F2g)}$[b]	Ratio decrease[b]	$I_{(Vo\text{-}Ce3+)}/I_{(F2g)}$	Area	Amp.	FWHM
1Pt/CA	0.68	/	0.41	/	/	4.81	0.12	26.5
1Pt/CZA	1.00	/	0.55	/	/	6.43	0.17	26.5
1Pt/CZA-T	1.12	/	0.68	/	/	6.28	0.20	24.7
1Pt/CA-a	0.34	50%	0.33	20%	/	/	/	/
1Pt/CZA-a	0.56	44%	0.45	18%	/	/	/	/
1Pt/CZA-T-a	0.81	28%	0.59	13%	/	/	/	/
CA	/	/	/	/	0.05	/	/	/
CZA	/	/	/	/	0.09	/	/	/
CZA-T	/	/	/	/	0.11	/	/	/

[a] Calculated by the peak area of Pt-O band ($I_{(Pt\text{-}O)}$) and CeO_2 F_{2g} band ($I_{(F2g)}$) in Raman spectra.
[b] Calculated by the peak area of Pt-O-Ce band ($I_{(Pt\text{-}O\text{-}Ce)}$) and CeO_2 F_{2g} band ($I_{(F2g)}$) in Raman spectra.

diffraction peaks for all the catalysts increased to a certain extent. Meanwhile, the full width at half maximum (FWHM) of the main CeO_2 (1 1 1) peak at *ca.* 28° decreased accordingly. The crystalline size of CeO_2 or $Ce_{0.9}Zr_{0.1}O_2$ was calculated by the Scherrer equation. As listed in Table 1, after aging treatment, the crystalline size of CeO_2 in 1Pt/CA increased from 10.8 to 12.5 nm, while it increased from 9.1 to 10.6 nm in 1Pt/CZA. Interestingly, only a slight increase of CeO_2 crystalline size has been observed for 1Pt/CZA-T (from 9.1 to 9.8 nm) after aging treatment, implying that 1Pt/CZA-T exhibited the best thermal stability to resist sintering although it already had the smallest crystalline size for CeO_2.

The BET surface areas (S_{BET}) were also measured for all the samples and listed in Table 1. CZA-T support exhibited a lower specific surface (85 m^2/g) than those of CZA (96 m^2/g) and CA (98 m^2/g) since 10CZA-800 was calcined at 800 °C in the preparation procedure. After the deposition of Pt, no apparent changes in the surface areas were observed for 1Pt/CZA-T, 1Pt/CZA and 1Pt/CA comparing to their corresponding supports. After the aging treatment, a significant drop in specific surface area was observed on 1Pt/CA (by 31 m^2/g) and 1Pt/CZA (by 22 m^2/g). For 1Pt/CZA-T, the drop was only by 9 m^2/g, suggesting higher thermal stability of 1Pt/CZA-T. Considering both XRD and S_{BET} results, it can be concluded that the Pt catalyst supported on CZA-T showed higher thermal stability than that on CA and CZA.

The XRD patterns of activated catalysts were also collected (Figs. 4b and S9b) to explore the effect of reduction treatment on the crystal structure of different supports. The XRD peak intensity for all catalysts decreased to a certain extent after activation treatment, while the FWHM of CeO_2 (1 1 1) peak slightly broadened, especially for 1Pt/CZA-a and 1Pt/CZA-T-a, implying that the crystallinity of CeO_2 or $Ce_{0.9}Zr_{0.1}O_x$ within these two catalysts slightly decreased due to H_2 reduction. For the 1Pt/CZA-T-a, the intensity of the CeO_2 diffraction peaks decreased most distinctly (from 9.1 to 8.1 nm, Table 1), which was mainly due to the highest dispersion of Pt on CZA-T and probably the strongest interaction between Pt and CeO_2 facilitating the most efficient reduction of CeO_2 by H_2. H_2-TPR is an effective approach to study the Pt-CeO_2 interaction by carefully examining the reduction peaks especially below 350 °C [40,41]. As the H_2-TPR results shown in Fig. S10a, the reduction peak of PtO_x and Pt-CeO_x on 1Pt/CZA-T was much broader and more intensive comparing to those on 1Pt/CA and 1Pt/CZA (centered at 125–138 °C), indicating that a deeper reduction was indeed achieved on 1Pt/CZA-T which correlated well with the XRD results. A more obvious and stronger reduction peak was observed at *ca.* 190 °C for 1Pt/CZA-T, which could be assigned to the reduction of CeO_2 entities strongly interacting with Pt species [42], further supporting the conclusion that Pt species was better dispersed and effectively anchored on CZA-T support. Due to the stronger binding between Pt single atoms and CZA-T, after the activation treatment under the same condition, Pt clusters with smaller size would form on 1Pt/CZA-T-a when compared with those on 1Pt/CZA-a and 1Pt/CA-a. H_2-TPR experiments were conducted on aged samples (1Pt/CZA-T-800A, 1Pt/CZA-800A and 1Pt/CA-800A) as well (Fig. S10b). The H_2-consumption peaks assigned to the reduction of Pt-O-Ce on 1Pt/CZA-T-800A still located at higher temperatures than those on 1Pt/CZA-800A and 1Pt/CA-800A, further suggesting the stronger Pt-O-Ce interaction on 1Pt/CZA-T-800A.

3.2.4. *Raman spectroscopy to determine surface defects and Pt-CeO_2 interaction*

The structural information such as metal-oxygen arrangement and surface defects of all the supports as well as catalysts before and after activation were investigated by Raman spectroscopy. The normalized Raman spectra of CA, CZA and CZA-T supports are shown in Fig. 4c. The intense bands at *ca.* 463 cm^{-1} could be assigned to the triply degenerate F_{2g} mode of fluorite-type CeO_2 lattice, while the band at *ca.* 610 cm^{-1} was attributed to the defect-induced mode due to the existence of oxygen vacancies in CeO_2 [43]. The relative concentration of surface defects was calculated from the peak area ratio of defect-induced mode to F_{2g} mode ($I_{(Vo\text{-}Ce3+)}/I_{(F2g)}$) and listed in Table 2. It was clear that the band at 610 cm^{-1} was strengthened after the doping of ZrO_2 into CeO_2, indicating that more oxygen vacancies were formed on CZA than on CA, which would probably be beneficial for oxygen activation and migration on CZA. For CZA-T support, the concentration of surface defects showed further increase comparing to CZA, proving again the benefit from the new T-IWI method resulting in smaller $Ce_{0.9}Zr_{0.1}O_2$ particles with more defective sites.

After the loading of Pt, two new vibration bands at 557 and 660 cm^{-1} could be observed (Fig. 4d), which could be assigned to Pt-O-Ce and Pt-O (in Pt-O-Ce) structures, respectively [30]. The abundant Pt-O-Ce and Pt-O species indicated that Pt was strongly bonded with CeO_2 support, supporting the existence of SMSI between Pt and supports. After H_2 activation, the amount of Pt-O-Ce and Pt-O species on 1Pt/CA-a, 1Pt/CZA-a and 1Pt/CZA-T-a declined to a certain extent comparing to as-prepared catalysts (Fig. S11). As already demonstrated in H_2-TPR results (Fig. S10), the H_2 consumption peaks below 400 °C were ascribed to the reduction of oxygen species bonded to Pt and adjacent Ce^{4+}. Therefore, the obvious decrease of Raman peak intensity for Pt-O-Ce and Pt-O species during the activation treatment suggested their facile reducibility to form catalytically active small Pt clusters.

To illustrate the intensity change of Pt-O-Ce and Pt-O bonds more clearly, the relative concentration of Pt-O-Ce and Pt-O structures on as-prepared and activated samples were calculated using the peak area ratios of $I_{(Pt\text{-}O\text{-}Ce)}/I_{(F2g)}$ and $I_{(Pt\text{-}O)}/I_{(F2g)}$, and the results are listed in Table 2. As can be clearly seen, the highest relative intensity of the band assigned to Pt-O and Pt-O-Ce structure was observed on 1Pt/CZA-T, suggesting the highest dispersion of Pt species on CZA-T support with the most intensive Pt-CeO_2 interaction. Interestingly, based on the peak area ratio decrease before and after activation, the reduction of Pt-O bond in 1Pt/CA catalyst (50%) was more intense than those in 1Pt/CZA (44%) and 1Pt/CZA-T (28%), a similar trend was also observed on Pt-O-Ce bond, which suggested that much higher portion of ionic Pt species had transformed into metallic Pt species in 1Pt/CA sample with

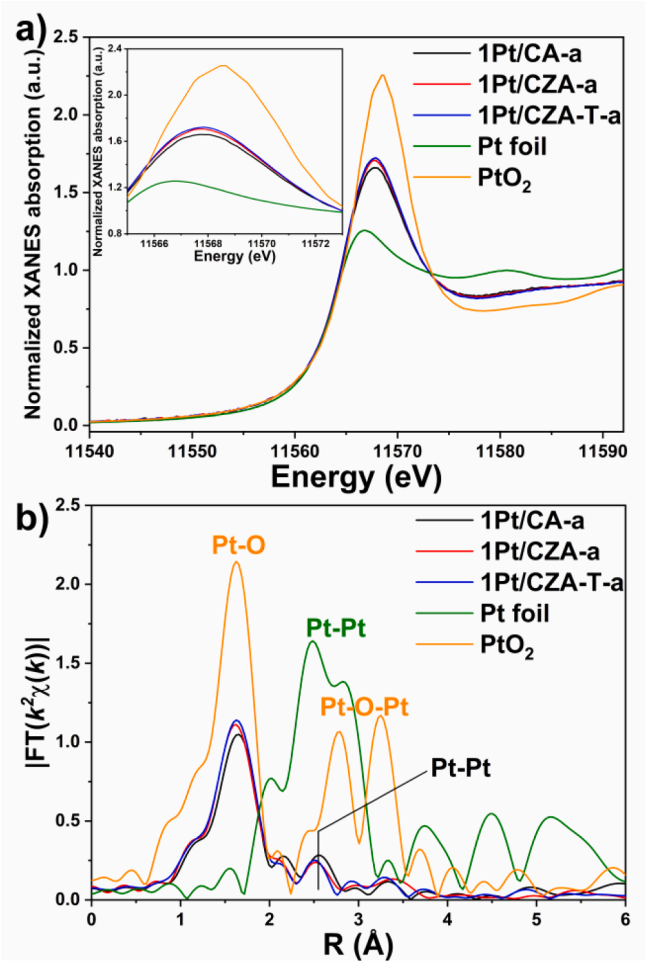

Fig. 5. a) Normalized XANES spectra and the b) EXAFS magnitude of the Fourier transformed k^2-weighted $\chi(k)$ data on 1Pt/CA-a, 1Pt/CZA-a and 1Pt/CZA-T-a at the Pt-L_3 edge. Reference samples of Pt foil and PtO_2 were used for comparison.

larger cluster or particle size. When combining the HAADT-STEM results with Raman spectra, it can be concluded that the final Pt cluster sizes on different supports after activation should be highly dependent on the initial intensity of Pt-O or Pt-O-Ce structure in as-prepared catalysts. Higher intensity of Pt-O or Pt-O-Ce structure and stronger interaction between Pt single sites and CeO_2 would lead to smaller and more homogeneously distributed Pt clusters after reduction treatment. Among three activated catalysts, there was a highest intensity of bands assigned Pt-O and Pt-O-Ce structures on 1Pt/CZA-T-a, indicating the smallest Pt clusters with the most fruitful Pt-CeO_2 interface on CZA-T support. This point of view can be further verified the XANES and EXAFS results for Pt-L_3 edge.

3.2.5. XANES and EXAFS analysis to determine Pt local structure

Using XAS technique, the nature of Pt species in different catalysts could be further well studied. As demonstrated by the Pt-L_3 XANES spectra of 1Pt/CA, 1Pt/CZA and 1Pt/CZA-T (Fig. S12a), the XANES patterns of these three samples were similar to that of PtO_2 but with slightly lower white line intensity, suggesting that the Pt species within these as-prepared samples was present in the valence state slightly lower than + 4. For all activated catalysts (Fig. 5a), the valence state of Pt species was greatly decreased but still between Pt^0 and Pt^{4+}. From the white line intensity, the Pt oxidation state on activated catalysts followed the sequence as: 1Pt/CZA-T-a > 1Pt/CZA-a > 1Pt/CA-a. As concluded earlier, smaller Pt clusters and more abundant Pt-CeO_2 interface could be formed on Pt/CZA-T-a, which meant that the reduced Pt clusters during the activation process within 1Pt/CZA-T-a was much easier to get re-oxidized once exposed to air again, correlating well with XANES results here.

To explore the local coordination structure of Pt species at atomic level, EXAFS curve fitting was conducted. As shown in Fig. S12b and Table S2 (with curve fitting results in R space and *k* space presented in Fig. S13), the typical exclusive Pt-O coordination environment and the absence of Pt-O-Pt/Pt-Pt structure on 1Pt/CA, 1Pt/CZA and 1Pt/CZA-T supported the view that the Pt species on as-prepared samples mainly existed in single site form. On activated catalysts, the Pt-Pt coordination structure was observed (Fig. 5b), confirming the formation of metallic Pt clusters. It was noteworthy that, on such activated catalysts, the coordination number (CN) of Pt-O followed the sequence as: 1Pt/CZA-T-a > 1Pt/CZA-a > 1Pt/CA-a, while the CN of Pt-Pt followed the sequence as: 1Pt/CZA-T-a ≈ 1Pt/CZA-a < 1Pt/CA-a (Table S2). As reported in literature, the lower CN of Pt-Pt always associated with smaller Pt clusters [44]. Therefore, in our case, the lower CN of Pt-Pt on 1Pt/CZA-T-a and 1Pt/CZA-a indicated that the Pt clusters on these two activated catalysts were indeed much smaller than that on 1Pt/CA-a. This was consistent with the HAADF-STEM results, where the average particle size of Pt clusters on activated catalysts followed the sequence as: 1Pt/CZA-T-a (1.1 ± 0.2 nm) < 1Pt/CZA-a (1.4 ± 0.3 nm) < 1Pt/CA-a (1.6 ± 0.4 nm). Furthermore, the higher CN of Pt-O indicated the formation of more PtO_x species, suggesting that the most abundant Pt-CeO_2 interfaces could be formed on 1Pt/CZA-T-a due to the smallest Pt cluster size induced by the unique CZA-T support.

3.3. XPS to determine surface chemical state

The Ce 3d XPS for all catalysts before and after activation as well as all different supports were deconvoluted into ten sub-peaks (Fig. 6). The peaks denoted as u and v were individually attributed to Ce $3d_{5/2}$ and Ce $3d_{3/2}$. Among those ten peaks, u^0, u', v^0 and v' were assigned to Ce^{3+} and the rest of them were related to Ce^{4+}. The relative surface concentration of Ce^{3+} was calculated from the following equation [45]:

$$Ce^{3+}(\%) = \frac{S_{v^0} + S_{v'} + S_{u^0} + S_{u'}}{\sum(S_v + S_u)}$$

where S_u and S_v were the intensity of peaks labeled as u and v, respectively.

As shown in Fig. 6a, by doping ZrO_2 into CeO_2, the surface Ce^{3+} concentration was increased from 26.0% on CA support to 28.4% on CZA support. Probably due to the high temperature (800 °C) calcination for 10CZA-800 preparation, the surface Ce^{3+} concentration on the final CZA-T support was actually decreased to 25.9% although it also showed very fine $Ce_{0.9}Zr_{0.1}O_2$ entities. It is interesting to see that, after the deposition of Pt onto different supports, a decline in the surface Ce^{3+} concentration was observed for all as-prepared catalysts, which could be the result of reaction between Ce^{3+} and PtO_2 to form Pt-O-Ce bonds [28]. After activation treatment, a notable enhancement of the intensity of u' and v' peaks for Ce^{3+} species could be observed for all catalysts, and the concentration of Ce^{3+} followed such sequence: 1Pt/CZA-T-a > 1Pt/CZA-a > 1Pt/CA-a. In the XRD section (Fig. 4b), it was found that 1Pt/CZA-T-a showed the most significant decrease in CeO_2 diffraction peaks after activation treatment, and such decrease in the CeO_2 crystallinity should associate with the formation of most abundant Ce^{3+} on CZA-T support. As reported in previous work, the formation of Ce^{3+} species was generally related to the generation of more oxygen defects on CeO_2 surface [46]. As discussed in Raman spectra and H_2-TPR sections, the strongest Pt-CeO_2 interaction and the most intensive reduction of Pt-CeO_x on 1Pt/CZA-T during the activation process (Fig. S10a) might account for the formation of its highest concentration of surface Ce^{3+} species. The highest concentration of surface Ce^{3+} and the resulted oxygen defects on 1Pt/CZA-T-a among the three catalysts could efficiently

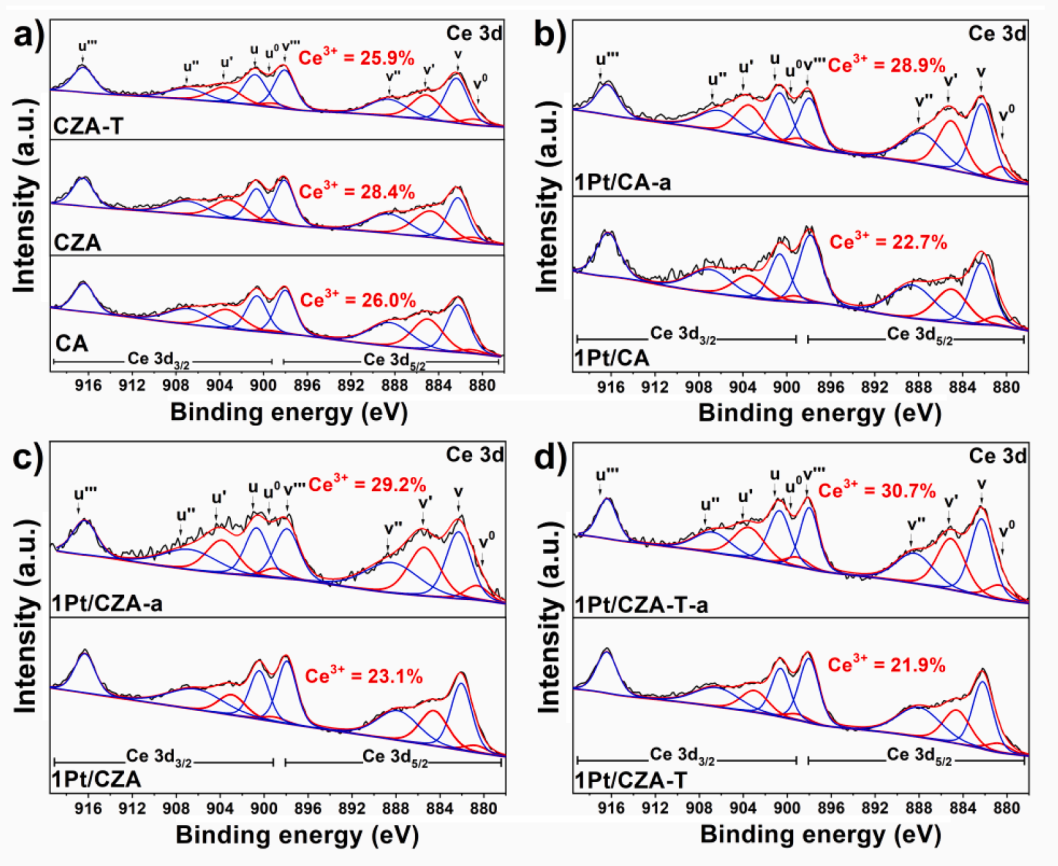

Fig. 6. XPS of Ce 3d for a) CA, CZA and CZA-T supports; b) 1Pt/CA, c) 1Pt/CZA and d) 1Pt/CZA-T catalysts before and after activation treatment.

facilitate the oxygen activation and oxygen transfer, thus ensuring its highest CO oxidation activity. It must be noted that XPS peaks of Pt 4f and Pt 4d overlap with Al 2p and Zr 3p, respectively, therefore, the Pt XPS and the surface composition could not be provided in this study.

3.4. OSC testing to determine oxygen activation/transfer capability

It has been widely reported that the CO oxidation on CeO_2-supported Pt catalysts followed a Mars-van Krevelen (MvK) mechanism where CO adsorbed on Pt species reacted with oxygen from CeO_2 lattice to form CO_2 [30,33,47–49]. Considering this, the CO oxidation activity of a CeO_2 supported Pt catalyst should be strongly correlated its ability of O_2 adsorption, activation and transfer. Dynamic OSC testing using cycling CO/O_2 pulses is an effective approach to characterize such properties of CeO_2-containing catalysts. The OSC testing was performed on both as-prepared and aged catalysts, and all catalysts were activated by H_2 at 400 °C for 1 h before testing. As shown in Fig. 7a, the OSC values on as-prepared catalysts followed the order of 1Pt/CZA-T-a > 1Pt/CZA-a > 1Pt/CA-a at all investigated temperatures (80–140 °C). The doping of ZrO_2 into CeO_2 could increase the OSC value of 1Pt/CA-a by *ca.* 20%, and by adopting the unique T-IWI method for CZA-T support preparation, the OSC value could be further improved.

It is well known that Zr^{4+} ion (86 pm) is smaller than Ce^{4+} ion (101 pm). When Zr^{4+} is introduced into CeO_2, more lattice defects could be created due to the lattice shrinking and strain [50]. It has been widely reported that the lattice defects were able to reduce the activation energy of lattice oxygen and enhance the oxygen mobility in CeO_2 bulk [51,52], which provides an explanation for the higher OSC on 1Pt/CZA-a and 1Pt/CZA-T-a than 1Pt/CA-a. Although CZA and CZA-T showed similar values of OSC (87 μmol $O{\cdot}g_{cat.}^{-1}$ at 300 °C, Fig. S14a), there was more promotion effect for the OSC function on CZA-T after Pt deposition. As already demonstrated in HAADF-STEM, XRD, Raman spectra and XAS results, more abundant and smaller $Ce_{0.9}Zr_{0.1}O_2$ entities with well dispersed Pt clusters could be formed on 1Pt/CZA-T-a. Such unique structures could contribute significantly to the enhanced OSC on 1Pt/CZA-T-a catalyst.

ZrO_2 doped CeO_2 is a common OSC material widely used in three-way catalysts (TWCs) for gasoline emission control. To compare the OSC function of 1Pt/CZA-T-a with conventional Pt/CeO_2-ZrO_2 materials, two types of CeO_2-ZrO_2 mixed oxides (Ce-Zr molar ratio as 9:1 and 6:4) were also prepared by a co-precipitation method followed by loading of 1 wt% Pt using IWI method (with obtained catalysts denoted as 1Pt/C9Z1 and 1Pt/C6Z4). As shown in Fig. 7b, 1Pt/CZA-T-a still possessed much higher OSC values than 1Pt/C9Z1-a and 1Pt/C6Z4-a. The superior OSC function and the much lower amount of $CeZrO_x$ used in 1Pt/CZA-T-a (only 30% of those in 1Pt/C9Z1-a and 1Pt/C6Z4-a) made 1Pt/CZA-T-a catalyst highly promising for automotive emission control in terms of both catalytic performance and cost-effectiveness.

After aging treatment, 1Pt/CZA-T-800A-a still showed higher OSC value than 1Pt/CA-800A-a and 1Pt/CZA-800A-a (Figs. S14b and c). To see the correlation between OSC function and CO oxidation activity, the CO reaction rates as a function of OSC values at 120 °C were plotted and shown in Fig. 7c. It can be clearly seen that the CO reaction rates on as-prepared and aged catalysts after activation were linearly correlated with their respective OSC values, indicating that the storage, activation and transfer of oxygen greatly determined the catalytic oxidation activity of Pt-based catalysts studied herein.

3.5. Reaction mechanism determined by in situ DRIFTS of CO Adsorption/Oxidation

In situ DRIFTS is a powerful tool to investigate the surface structure of

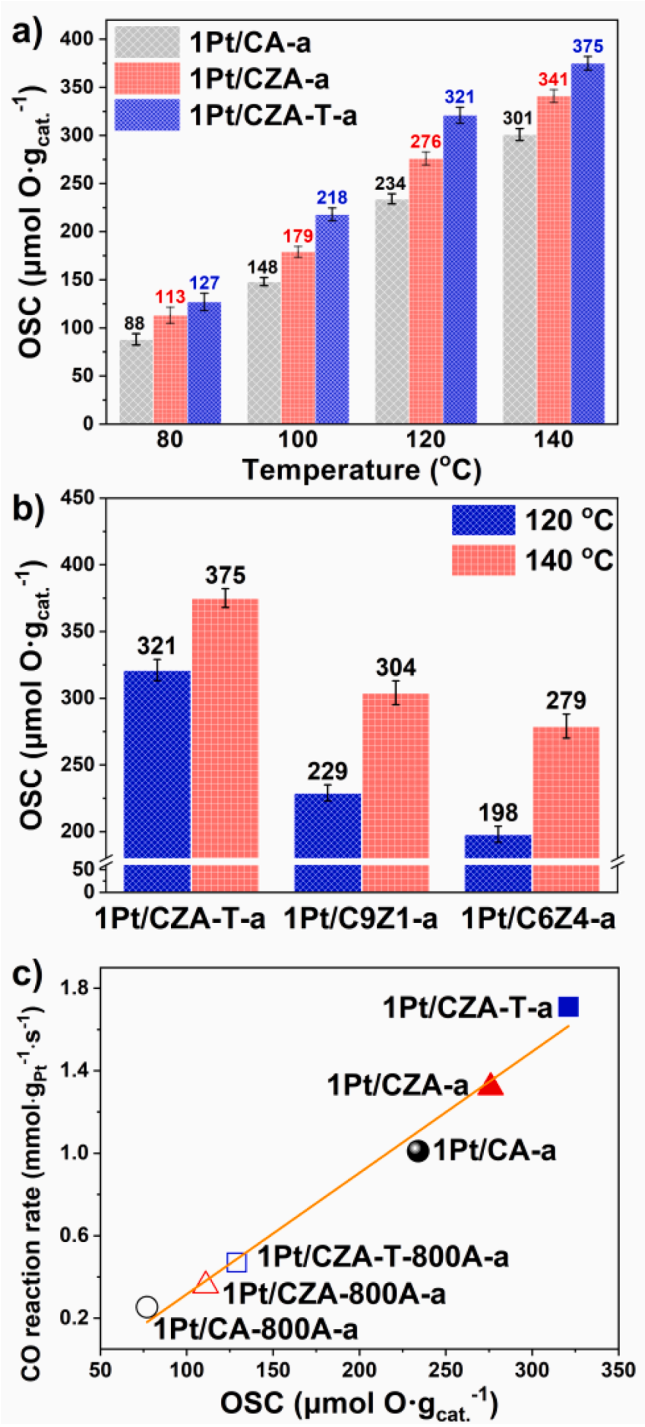

Fig. 7. OSC values of a) 1Pt/CA-a, 1Pt/CZA-a and 1Pt/CZA-T-a catalysts tested at different temperatures, and OSC values of b) 1Pt/CZA-T-a, 1Pt/C9Z1-a and 1Pt/C6Z4-a catalysts tested at 120/140 °C. c) Linear relationship between the OSC values and CO reaction rates at 120 °C on fresh and aged 1Pt/CA, 1Pt/CZA and 1Pt/CZA-T catalysts after activation.

a catalyst via monitoring the adsorption of probe molecules. To further explore the initial dispersion state of Pt species on different supports, *in situ* DRIFTS of CO adsorption at 25 °C was performed on 1Pt/CA, 1Pt/CZA and 1Pt/CZA-T catalysts. As shown in Fig. 8a–c, over all three catalysts, a well-defined peak at *ca.* 2098 cm^{-1} could be observed, which could be assigned to CO adsorbed on ionic Pt species corresponding to Pt single sites (CO-$Pt^{\delta+}$@Pt_1) on CA, CZA and CZA-T supports [4]. However, the intensity and FWHM of the peak at 2098 cm^{-1} varied significantly for the three catalysts (Table 2). The CO adsorption peak on 1Pt/CZA-T catalyst showed the minimum FWHM among the three, suggesting a most homogeneous coordination environment of Pt single sites on CZA-T support. For 1Pt/CZA and 1Pt/CA, a similar FWHM was detected. However, the CO adsorption peak on 1Pt/CZA was much more intense than that on 1Pt/CA, indicating that more exposed Pt single sites were present on CZA surface. It was also noticed that, in Ar or O_2 flow, the intensity of the band assigned to CO-$Pt^{\delta+}$@Pt_1 minimally changed even at temperatures up to 100 °C (Fig. S15). These results indicated that CO was over-strongly bound to Pt single sites (CO poisoning effect), which resulted in the limited activity for 1Pt/CA, 1Pt/CZA and 1Pt/CZA-T for CO oxidation at low temperatures [30]. In other words, ionic Pt single sites on catalysts without activation were not active for CO oxidation at least at low temperature, which correlated well with previous CO oxidation results.

In order to further determine the true active sites, the DRIFTS spectra for CO adsorption on 1Pt/CA-a, 1Pt/CZA-a and 1Pt/CZA-T-a at 25 °C were collected and shown in Fig. 8d–f. Three CO adsorption bands were observed on the activated catalysts. In addition to the bands at *ca.* 2100 cm^{-1} assignable to CO adsorbed on ionic Pt sites (CO-$Pt^{\delta+}$@PtO_x), new bands at *ca.* 2084 cm^{-1} and *ca.* 2066 cm^{-1} were also observed on activated catalysts, which could be assigned to CO linearly adsorbed on the terrace sites of metallic Pt clusters (well-coordinated Pt sites) and step/corner sites of metallic Pt clusters (under-coordinated Pt sites), respectively [30,53–55]. The CO adsorbed on metallic Pt clusters was denoted as CO-Pt^0@cluster. Although all the activated catalysts presented three types of Pt species, the band intensities for CO adsorption on these catalysts were totally different. The band of CO-Pt^0@cluster on 1Pt/CZA-T-a was most intense, indicating the most abundant Pt cluster sites on this activated catalyst. As illustrated in Fig. 8g–i, the intensities of the bands attributed to CO-Pt^0@cluster decreased dramatically after the introduction of O_2 into the stream at 50 °C, which meant that CO adsorbed on metallic Pt clusters were highly reactive species during the CO oxidation reaction. Cargnello et al. has found that the CO oxidation performance on CeO_2 supported catalysts could be significantly enhanced at metal-CeO_2 interfacial sites for VIII metal catalysts [56]. On 1Pt/CZA-T-a catalyst, the presence of most abundant small Pt clusters, the formation of richest Pt-CeO_2 interface, and the highest concentration of surface Ce^{3+}/oxygen defects significantly contributed to its highest OSC function and CO oxidation activity among all the activated catalysts. And it would be discussed in detail later.

The H_2O effect on the catalytic performance of 1Pt/CZA-T-a was investigated by *in situ* DRIFTS of O_2 reacting with pre-adsorbed CO on H_2O-treated 1Pt/CZA-T-a (air with 10 vol% H_2O at 100 °C for 1 h). As shown in Fig. S16, the reactivity of CO adsorbed on metallic Pt sites was promoted after H_2O treatment, suggesting that the adsorbed −OH/H_2O could facilitate the CO oxidation reaction on 1Pt/CZA-T-a catalyst.

The stability of Pt clusters on 1Pt/CZA-T-a was well verified by *in situ* DRIFTS of CO oxidation experiments conducted at 50 and 100 °C (Figs. S17 and S18). The superior stability of active Pt species on 1Pt/CZA-T-a was also demonstrated by a cycling CO oxidation test from room temperature to 300 °C in the presence of 5 vol% H_2O (Fig. S19), where the CO oxidation activity on 1Pt/CZA-T-a and 1Pt/CZA-a showed no obvious decrease even after 3 cycles (with 1Pt/CZA-T-a always outperforming 1Pt/CZA-a). To further investigate the stability of Pt clusters on activated aged samples, *in situ* DRIFTS of CO adsorption was also conducted on fresh 1Pt/CZA-T-800A-a and 1Pt/CZA-800A-a, as well as spent 1Pt/CZA-T-800A-a and 1Pt/CZA-800A-a (which was exposed to CO + O_2 reaction flow at 200 °C for 1 h) for comparison (Fig. S20). It was found that Pt clusters on 1Pt/CZA-T-800A-a indeed showed better stability than those on 1Pt/CZA-800A-a. These results suggested that the CZA-T support favored the higher stability of Pt clusters.

3.6. Relationship between catalytic performance and catalyst properties

To reveal the relationship between catalyst structure and CO

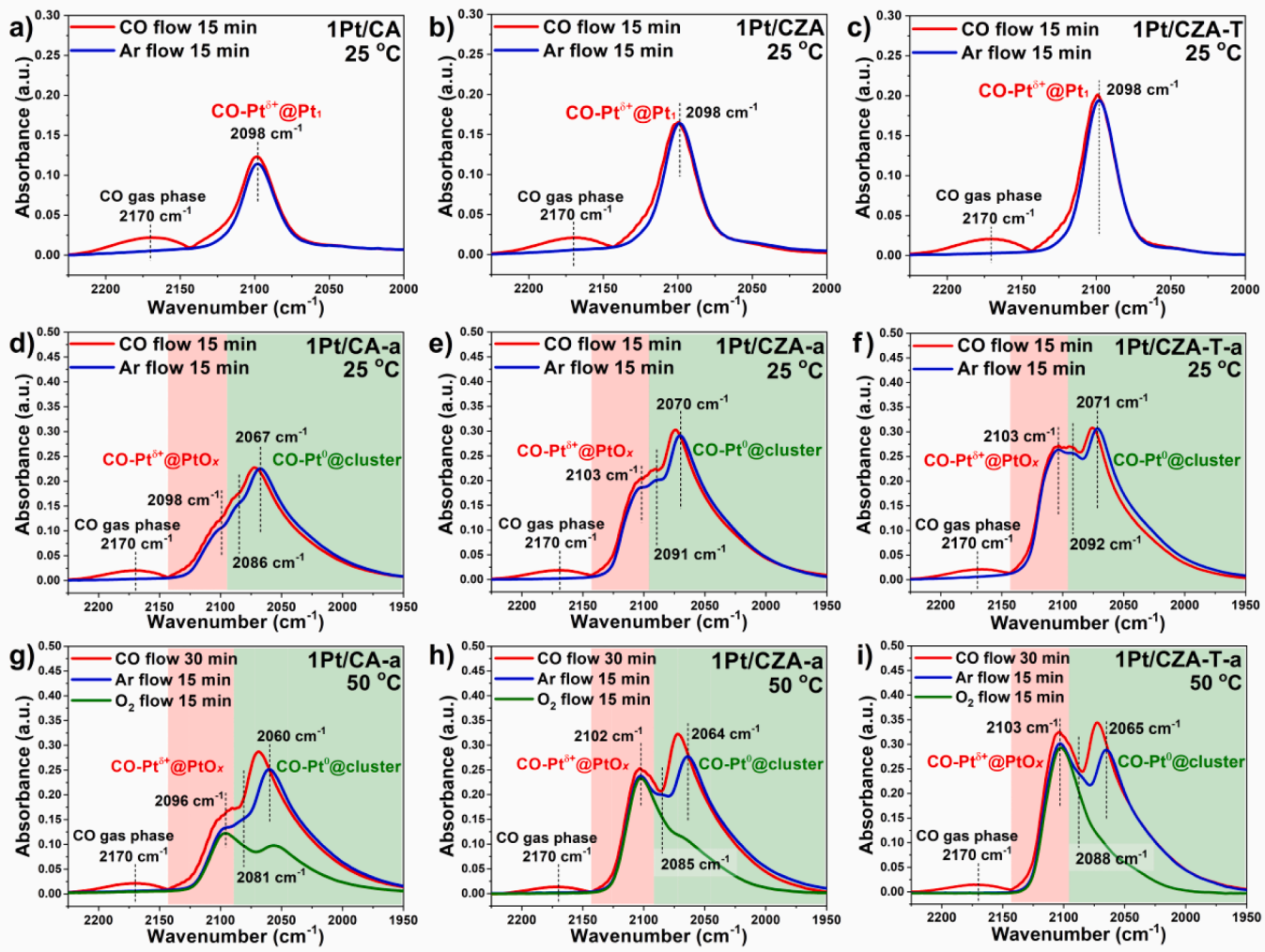

Fig. 8. *In situ* DRIFTS of CO adsorption on a) 1Pt/CA, b) 1Pt/CZA, c) 1Pt/CZA-T, d) 1Pt/CA-a, e) 1Pt/CZA-a and f) 1Pt/CZA-T-a at 25 °C; *In situ* DRIFTS of O_2 reacting with pre-adsorbed CO on g) 1Pt/CA-a, h) 1Pt/CZA-a and i) 1Pt/CZA-T-a at 50 °C (Ar purge for 15 min before the injection of O_2).

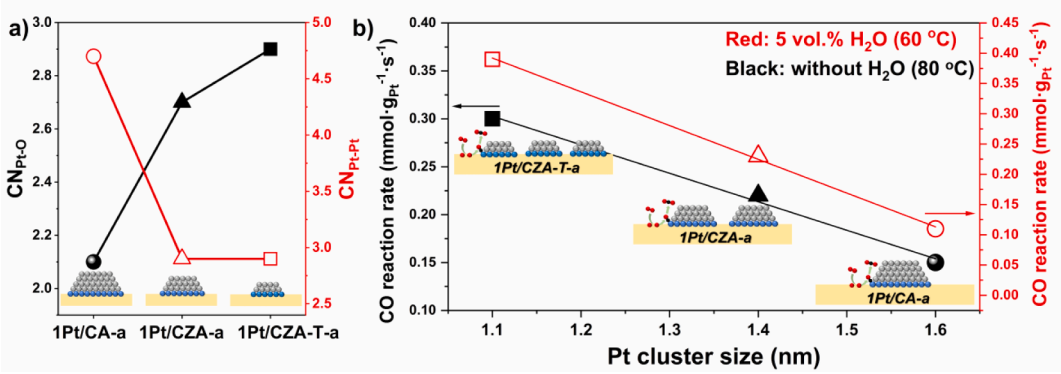

Fig. 9. The relationship between a) Pt cluster sizes and the results of XAS analysis; b) CO reaction rates (with 5 vol% H_2O in the reactants at 60 °C and without H_2O in the reactants at 80 °C) and Pt cluster sizes determined by HAADF-STEM.

oxidation activity, the results of CO oxidation rates, Pt cluster sizes determined by HAADF-STEM, and XAS results were rearranged and presented in Fig. 9. In XAS analysis section, the coordination number (CN) of Pt-Pt and Pt-O were directly related to the size of Pt clusters on different supports. Pt clusters with smaller particle size showed higher CN_{Pt-O} and lower CN_{Pt-Pt} (Fig. 9a), which was well supported by the results of Raman spectra (Table 2, Fig. S11), *in situ* DRIFTS of CO adsorption (Fig. 8) and HAADF-STEM results (Fig. 3). As illustrated in Fig. 9b, the CO oxidation activity (with or without 5 vol% H_2O in the reactant stream) of as-prepared catalysts after activation was highly related to the size of Pt clusters, where the catalyst possessing smaller Pt clusters with more active sites at Pt-CeO_2 interface exhibited higher CO oxidation activity.

To further investigate the role of Pt-CeO_2 perimeter sites in CO

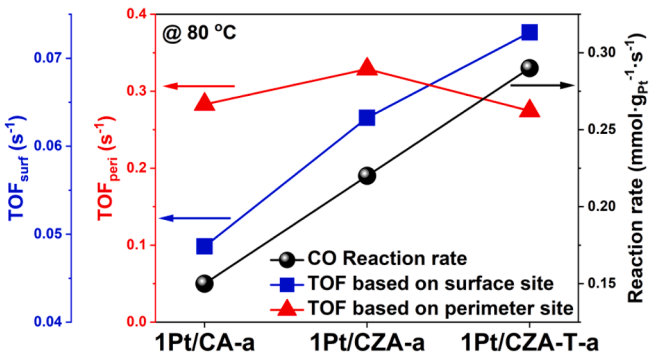

Fig. 10. CO reaction rate, TOF_{surf} and TOF_{peri} on 1Pt/CZA-T-a, 1Pt/CZA-a and 1Pt/CA-a in CO oxidation reaction at 80 °C.

oxidation activity, the turnover frequency (TOF) based on the number of surface exposed Pt sites (TOF_{surf}) and the number of perimeter Pt sites (TOF_{peri}) was calculated. The details of the calculation can be found in Text S1 and Table S3 in Supporting Information. As shown in Fig. 10, although the TOF_{surf} on 1Pt/CZA-T-a was higher than that on 1Pt/CZA-a and 1Pt/CA-a, the TOF_{peri} was almost the same on these three catalysts. More perimeter sites on 1Pt/CZA-T-a could facilitate the activation of oxygen, and the activated oxygen could efficiently react with CO adsorbed on metallic Pt sites of Pt clusters. Therefore, 1Pt/CZA-T-a exhibited the best CO oxidation activity, which was well supported by the reports that the ceria perimeter sites at the noble metal-support interface in combination with CO covered and thus reduced Pt particles are crucial to enable a fast reaction pathway at low temperature [57]. More perimeter sites and relatively higher concentration of surface Ce^{3+} on 1Pt/CZA-T-a also well explained its higher dynamic OSC function.

4. Conclusion

A novel CeO_2-ZrO_2/Al_2O_3 support (CZA-T) with fine $Ce_{0.9}Zr_{0.1}O_2$ particles was successfully synthesized by the two-step incipient wetness impregnation (T-IWI) method. The fine $Ce_{0.9}Zr_{0.1}O_2$ particles on CZA-T favored the Pt species to be highly dispersed and strongly anchored in single site form. Although 1Pt/CZA-T showed the lowest initial CO oxidation activity among the studied catalysts, after H_2 reduction activation, 1Pt/CZA-T-a showed the highest catalytic performance in CO and C_3H_8 oxidation. Smaller homogeneous Pt clusters were formed on 1Pt/CZA-T-a comparing to those on 1Pt/CA-a and 1Pt/CZA-a resulted from conventional one-step IWI method. As a result, more Pt-CeO_2 perimeter sites were formed on 1Pt/CZA-T-a, which contributed to its higher OSC function and catalytic oxidation performance. Furthermore, 1Pt/CZA-T also showed superior thermal stability. This work provides a new design strategy for the cost-effective Pt/CeO_2-based catalysts with better catalytic oxidation performance and lower CeO_2 usage for more efficient industrial applications.

Declaration of Competing Interest

The authors declare that they have no known competing financial interests or personal relationships that could have appeared to influence the work reported in this paper.

Acknowledgements

F. G. acknowledges the support from the National Natural Science Foundation of China (No. 21972063) and Natural Science Foundation of Jiangsu Province (BK20200012). F. L. acknowledges Startup Fund from the University of Central Florida (UCF). S. X. thanks the support from the Preeminent Postdoctoral Program (P3) at UCF. F. L. sincerely thanks Dr. Marcos Schöneborn at Sasol for providing raw materials in catalyst synthesis. This research used beamline 7-BM (QAS) of the National Synchrotron Light Source II, a U.S. Department of Energy (DOE) Office of Science User Facility operated for the DOE Office of Science by Brookhaven National Laboratory under Contract No. DE-SC0012704. The authors thank Mr. Corbin Feit and Prof. Titel Jurca at UCF for the water contact angle measurement.

Appendix A. Supplementary data

Supplementary data to this article can be found online at https://doi.org/10.1016/j.cej.2021.131855.

References

[1] A.K. Datye, M. Votsmeier, Opportunities and challenges in the development of advanced materials for emission control catalysts, Nat. Mater. 20 (2021) 1049–1059.
[2] P. Iodice, A. Senatore, G. Langella, A. Amoresano, Effect of ethanol-gasoline blends on CO and HC emissions in last generation SI engines within the cold-start transient: an experimental investigation, Appl. Energy 179 (2016) 182–190.
[3] A.M. Gänzler, M. Casapu, P. Vernoux, S. Loridant, F.J. Cadete Santos Aires, T. Epicier, B. Betz, R. Hoyer, J.D. Grunwaldt, Tuning the structure of platinum particles on ceria in situ for enhancing the catalytic performance of exhaust gas catalysts, Angew. Chem. Int. Ed. 56 (2017) 13078–13082.
[4] J. Jones, H. Xiong, A.T. DeLaRiva, E.J. Peterson, H. Pham, S.R. Challa, G. Qi, S. Oh, M.H. Wiebenga, X.I.P. Hernández, Thermally stable single-atom platinum-on-ceria catalysts via atom trapping, Science 353 (2016) 150–154.
[5] L. Nie, D. Mei, H. Xiong, B. Peng, Z. Ren, X.I.P. Hernandez, A. DeLaRiva, M. Wang, M.H. Engelhard, L. Kovarik, Activation of surface lattice oxygen in single-atom Pt/CeO_2 for low-temperature CO oxidation, Science 358 (2017) 1419–1423.
[6] E. Slavinskaya, R. Gulyaev, A. Zadesenets, O. Stonkus, V. Zaikovskii, Y.V. Shubin, S. Korenev, A. Boronin, Low-temperature CO oxidation by Pd/CeO_2 catalysts synthesized using the coprecipitation method, Appl. Catal. B 166 (2015) 91–103.
[7] H. Xiong, M.H. Wiebenga, C. Carrillo, J.R. Gaudet, H.N. Pham, D. Kunwar, S.H. Oh, G. Qi, C.H. Kim, A.K. Datye, Design considerations for low-temperature hydrocarbon oxidation reactions on Pd based catalysts, Appl. Catal. B 236 (2018) 436–444.
[8] J. Lee, Y. Ryou, X. Chan, T.J. Kim, D.H. Kim, How Pt interacts with CeO_2 under the reducing and oxidizing environments at elevated temperature: the origin of improved thermal stability of Pt/CeO_2 compared to CeO_2, J. Phys. Chem. C 120 (2016) 25870–25879.
[9] B.M. Reddy, A. Khan, Nanosized CeO_2-SiO_2, CeO_2-TiO_2, and CeO_2-ZrO_2 mixed oxides: influence of supporting oxide on thermal stability and oxygen storage properties of ceria, Catal. Surv. from Asia 9 (2005) 155–171.
[10] J. Zhu, L. Zhang, Y. Deng, B. Liu, L. Dong, F. Gao, K. Sun, L. Dong, Y. Chen, Influence of preparation method on the catalytic activities of CuO/$Ce_{0.67}Zr_{0.33}O_2$ catalysts in CO + O_2 reaction, Appl. Catal. B 96 (2010) 449–457.
[11] Z. Abbasi, M. Haghighi, E. Fatehifar, S. Saedy, Synthesis and physicochemical characterizations of nanostructured Pt/Al_2O_3-CeO_2 catalysts for total oxidation of VOCs, J. Hazard. Mater. 186 (2011) 1445–1454.
[12] H.-P. Zhou, H.-S. Wu, J. Shen, A.-X. Yin, L.-D. Sun, C.-H. Yan, Thermally stable Pt/CeO_2 hetero-nanocomposites with high catalytic activity, J. Am. Chem. Soc. 132 (2010) 4998–4999.
[13] H. Wang, J.-X. Liu, L.F. Allard, S. Lee, J. Liu, H. Li, J. Wang, J. Wang, S.H. Oh, W. Li, M. Flytzani-Stephanopoulos, M. Shen, B.R. Goldsmith, M. Yang, Surpassing the single-atom catalytic activity limit through paired Pt-O-Pt ensemble built from isolated Pt_1 atoms, Nat. Commun. 10 (2019) 3808.
[14] K. Khivantsev, C.G. Vargas, J. Tian, L. Kovarik, N.R. Jaegers, J. Szanyi, Y. Wang, Economizing on Precious Metals in three-way catalysts: thermally stable and highly active single-atom rhodium on ceria for NO abatement under dry and industrially relevant conditions, Angew. Chem. Int. Ed. 60 (2021) 391.
[15] A. Santos, S. Damyanova, G. Teixeira, L.V. Mattos, F.B. Noronha, F.B. Passos, J. Bueno, The effect of ceria content on the performance of Pt/CeO_2/Al_2O_3 catalysts in the partial oxidation of methane, Appl. Catal. A 290 (2005) 123–132.
[16] L. Li, N. Zhang, R. Wu, L. Song, G. Zhang, H. He, Comparative study of moisture-treated Pd@CeO_2/Al_2O_3 and Pd/CeO_2/Al_2O_3 catalysts for automobile exhaust emission reactions: effect of core-shell interface, ACS Appl. Mater. Interfaces 12 (2020) 10350–10358.
[17] H. Jeong, O. Kwon, B.-S. Kim, J. Bae, S. Shin, H.-E. Kim, J. Kim, H. Lee, Highly durable metal ensemble catalysts with full dispersion for automotive applications beyond single-atom catalysts, Nat. Catal. 3 (2020) 368–375.
[18] L. Lan, X. Huang, W. Zhou, H. Li, J. Xiang, S. Chen, Y. Chen, Development of a thermally stable Pt catalyst by redispersion between CeO_2 and Al_2O_3, RSC Adv. 11 (2021) 7015–7024.
[19] R. Di Monte, P. Fornasiero, J. Kašpar, M. Graziani, J.M. Gatica, S. Bernal, A. Gómez-Herrero, Stabilisation of nanostructured $Ce_{0.2}Zr_{0.8}O_2$ solid solution by impregnation on Al_2O_3: a suitable method for the production of thermally stable oxygen storage/release promoters for three-way catalysts, Chem. Commun. (2000) 2167–2168, https://doi.org/10.1039/b006674p.
[20] A. Trovarelli, Catalytic properties of ceria and CeO_2-containing materials, Catal. Rev. Sci. Eng. 38 (1996) 439–520.

[21] Y. Feng, Q. Wan, H. Xiong, S. Zhou, X. Chen, X.I. Pereira Hernandez, Y. Wang, S. Lin, A.K. Datye, H. Guo, Correlating DFT calculations with CO oxidation reactivity on Ga-doped Pt/CeO_2 single-atom catalysts, J. Phys. Chem. C 122 (2018) 22460–22468.

[22] S. Rossignol, C. Descorme, C. Kappenstein, D. Duprez, Synthesis, structure and catalytic properties of Zr-Ce-Pr-O mixed oxides, J. Mater. Chem. C 11 (2001) 2587–2592.

[23] R. Si, Y.-W. Zhang, L.-M. Wang, S.-J. Li, B.-X. Lin, W.-S. Chu, Z.-Y. Wu, C.-H. Yan, Enhanced thermal stability and oxygen storage capacity for $Ce_xZr_{1-x}O_2$ (x = 0.4-0.6) solid solutions by hydrothermally homogenous doping of trivalent rare earths, J. Phys. Chem. C 111 (2007) 787–794.

[24] C.E. Hori, H. Permana, K.S. Ng, A. Brenner, K. More, K.M. Rahmoeller, D. Belton, Thermal stability of oxygen storage properties in a mixed CeO_2-ZrO_2 system, Appl. Catal., B 16 (1998) 105–117.

[25] F. Zhang, Z. Liu, X. Chen, N. Rui, L.E. Betancourt, L. Lin, W. Xu, C.-J. Sun, A. M. Abeykoon, J.A. Rodriguez, The effects of Zr-doping into ceria for the dry reforming of methane over Ni/$CeZrO_2$ catalysts: In-situ studies with XRD, XAFS and AP-XPS, ACS Catal 10 (2020) 3274–3284.

[26] B. Liu, C. Li, G. Zhang, X. Yao, S.S.C. Chuang, Z. Li, Oxygen vacancy promoting dimethyl carbonate synthesis from CO_2 and methanol over Zr-doped CeO_2 nanorods, ACS Catal. 8 (2018) 10446–10456.

[27] P. Sudarsanam, B. Mallesham, P.S. Reddy, D. Großmann, W. Grünert, B.M. Reddy, Nano-Au/CeO_2 catalysts for CO oxidation: Influence of dopants (Fe, La and Zr) on the physicochemical properties and catalytic activity, Appl. Catal., B 144 (2014) 900–908.

[28] D. Kunwar, S. Zhou, A. DeLaRiva, E.J. Peterson, H. Xiong, X.I. Pereira-Hernández, S.C. Purdy, R. ter Veen, H.H. Brongersma, J.T. Miller, H. Hashiguchi, L. Kovarik, S. Lin, H. Guo, Y. Wang, A.K. Datye, Stabilizing high metal loadings of thermally stable platinum single atoms on an industrial catalyst support, ACS Catal. 9 (5) (2019) 3978–3990.

[29] X. Ye, H. Wang, Y. Lin, X. Liu, L. Cao, J. Gu, J. Lu, Insight of the stability and activity of platinum single atoms on ceria, Nano Res. 12 (2019) 1401–1409.

[30] X.I. Pereira-Hernández, A. DeLaRiva, V. Muravev, D. Kunwar, H. Xiong, B. Sudduth, M. Engelhard, L. Kovarik, E.J.M. Hensen, Y. Wang, A.K. Datye, Tuning Pt-CeO_2 interactions by high-temperature vapor-phase synthesis for improved reducibility of lattice oxygen, Nat. Commun. 10 (2019) 1358.

[31] M. González-Castaño, S. Ivanova, O.H. Laguna, L.M. Martínez T., M.A. Centeno, J. A. Odriozola, Structuring Pt/CeO_2/Al_2O_3 WGS catalyst: introduction of buffer layer, Appl. Catal., B 200 (2017) 420–427.

[32] K. Xie, Y. Xiao, H. Li, Activating lattice oxygen at twisted surface in mesoporous CeO_2 single crystal for efficient and durable catalytic CO oxidation, Angew. Chem. Int. Ed. 60 (2021) 5240–5244.

[33] C. Wang, X.-K. Gu, H. Yan, Y. Lin, J. Li, D. Liu, W.-X. Li, J. Lu, Water-mediated Mars-Van Krevelen mechanism for CO oxidation on ceria-supported single-atom Pt_1 catalyst, ACS Catal. 7 (2017) 887–891.

[34] H. Ha, S. Yoon, K. An, H.Y. Kim, Catalytic CO oxidation over Au nanoparticles supported on CeO_2 nanocrystals: effect of the Au-CeO_2 interface, ACS Catal. 8 (2018) 11491–11501.

[35] H. Tan, J. Wang, S. Yu, K. Zhou, Support morphology-dependent catalytic activity of Pd/CeO_2 for formaldehyde oxidation, Environ. Sci. Technol. 49 (2015) 8675–8682.

[36] F. Dvořák, M. Farnesi Camellone, A. Tovt, N.-D. Tran, F.R. Negreiros, M. Vorokhta, T. Skála, I. Matolínová, J. Mysliveček, V. Matolín, S. Fabris, Creating single-atom Pt-ceria catalysts by surface step decoration, Nat. Commun. 7 (2016) 10801.

[37] P. Losch, W. Huang, O. Vozniuk, E.D. Goodman, W. Schmidt, M. Cargnello, Modular Pd/Zeolite composites demonstrating the key role of support hydrophobic/hydrophilic character in methane catalytic combustion, ACS Catal. 9 (2019) 4742–4753.

[38] C. Morterra, V. Bolis, G. Magnacca, Surface characterization of modified aluminas. Part 4. surface hydration and lewis acidity of CeO_2-Al_2O_3 systems, J. Chem. Soc., Faraday Trans. 92 (1996) 1991–1999.

[39] M. Fronzi, M.H.N. Assadi, D.A.H. Hanaor, Theoretical insights into the hydrophobicity of low index CeO_2 surfaces, Appl. Surf. Sci. 478 (2019) 68–74.

[40] E.A. Derevyannikova, T.Y. Kardash, A.I. Stadnichenko, O.A. Stonkus, E. M. Slavinskaya, V.A. Svetlichnyi, A.I. Boronin, Structural insight into strong Pt-CeO_2 interaction: from single Pt atoms to PtO_x clusters, J. Phys. Chem. C 123 (2019) 1320–1334.

[41] X. Tang, B. Zhang, Y. Li, Y. Xu, Q. Xin, W. Shen, Structural features and catalytic properties of Pt/CeO_2 catalysts prepared by modified reduction-deposition techniques, Catal Lett. 97 (2004) 163–169.

[42] Y. Gao, W. Wang, S. Chang, W. Huang, Morphology effect of CeO_2 support in the preparation, metal-support interaction, and catalytic performance of Pt/CeO_2 catalysts, ChemCatChem 5 (2013) 3610–3620.

[43] S. Loridant, Raman spectroscopy as a powerful tool to characterize ceria-based catalysts, Catal. Today 373 (2021) 98–111.

[44] A. Liu, X. Liu, L. Liu, Y. Pu, K. Guo, W. Tan, S. Gao, Y. Luo, S. Yu, R. Si, B. Shan, F. Gao, L. Dong, Getting insights into the temperature-specific active sites on platinum nanoparticles for CO oxidation: a combined in situ spectroscopic and ab initio density functional theory study, ACS Catal. 9 (2019) 7759–7768.

[45] L. Qi, Q. Yu, Y. Dai, C. Tang, L. Liu, H. Zhang, F. Gao, L. Dong, Y. Chen, Influence of cerium precursors on the structure and reducibility of mesoporous CuO-CeO_2 catalysts for CO oxidation, Appl. Catal. B 119-120 (2012) 308–320.

[46] P. Dutta, S. Pal, M.S. Seehra, Y. Shi, E.M. Eyring, R.D. Ernst, Concentration of Ce^{3+} and oxygen vacancies in cerium oxide nanoparticles, Chem. Mater. 18 (2006) 5144–5146.

[47] H.-H. Liu, Y. Wang, A.-P. Jia, S.-Y. Wang, M.-F. Luo, J.-Q. Lu, Oxygen vacancy promoted CO oxidation over Pt/CeO_2 catalysts: a reaction at Pt-CeO_2 interface, Appl. Surf. Sci. 314 (2014) 725–734.

[48] F. Morfin, T.-S. Nguyen, J.-L. Rousset, L. Piccolo, Synergy between hydrogen and ceria in Pt-catalyzed CO oxidation: an investigation on Pt-CeO_2 catalysts synthesized by solution combustion, Appl. Catal. B 197 (2016) 2–13.

[49] R. Kopelent, J.A. van Bokhoven, J. Szlachetko, J. Edebeli, C. Paun, M. Nachtegaal, O.V. Safonova, Catalytically active and spectator Ce^{3+} in ceria-supported metal catalysts, Angew. Chem. Int. Ed. 54 (30) (2015) 8728–8731.

[50] X. Yao, C. Tang, Z. Ji, Y. Dai, Y. Cao, F. Gao, L. Dong, Y. Chen, Investigation of the physicochemical properties and catalytic activities of $Ce_{0.67}M_{0.33}O_2$ (M = Zr^{4+}, Ti^{4+}, Sn^{4+}) solid solutions for NO removal by CO, Catal. Sci. Technol. 3 (2013) 688–698.

[51] S. Bedrane, C. Descorme, D. Duprez, Investigation of the oxygen storage process on ceria-and ceria-zirconia-supported catalysts, Catal. Today 75 (2002) 401–405.

[52] P. Vidmar, P. Fornasiero, J. Kašpar, G. Gubitosa, M. Graziani, Effects of trivalent dopants on the redox properties of $Ce_{0.6}Zr_{0.4}O_2$ mixed oxide, J. Catal. 171 (1997) 160–168.

[53] K. Ding, A. Gulec, A.M. Johnson, N.M. Schweitzer, G.D. Stucky, L.D. Marks, P. C. Stair, Identification of active sites in CO oxidation and water-gas shift over supported Pt catalysts, Science 350 (2015) 189–192.

[54] O. Pozdnyakova, D. Teschner, A. Wootsch, J. Kröhnert, B. Steinhauer, H. Sauer, L. Toth, F.C. Jentoft, A. Knop-Gericke, Z. Paál, R. Schlögl, Preferential CO oxidation in hydrogen (PROX) on ceria-supported catalysts, part I: oxidation state and surface species on Pt/CeO_2 under reaction conditions, J. Catal. 237 (2006) 1–16.

[55] T. Avanesian, S. Dai, M.J. Kale, G.W. Graham, X. Pan, P. Christopher, Quantitative and atomic-scale view of CO-induced Pt nanoparticle surface reconstruction at saturation coverage via DFT calculations coupled with in situ TEM and IR, J. Am. Chem. Soc. 139 (2017) 4551–4558.

[56] M. Cargnello, V.V. Doan-Nguyen, T.R. Gordon, R.E. Diaz, E.A. Stach, R.J. Gorte, P. Fornasiero, C.B. Murray, Control of metal nanocrystal size reveals metal-support interface role for ceria catalysts, Science 341 (2013) 771–773.

[57] A.M. Gänzler, M. Casapu, D.E. Doronkin, F. Maurer, P. Lott, P. Glatzel, M. Votsmeier, O. Deutschmann, J.-D. Grunwaldt, Unravelling the different reaction pathways for low temperature CO oxidation on Pt/CeO_2 and Pt/Al_2O_3 by spatially resolved structure-activity correlations, J. Phys. Chem. Lett. 10 (2019) 7698–7705.